

## Article

# Computational Fluid Dynamics-Based Optimisation of High-Speed and High-Performance Bearingless Cross-Flow Fan Designs

Ivana Bagaric <sup>1,\*</sup> , Daniel Steinert <sup>2</sup> , Thomas Nussbaumer <sup>2</sup>  and Johann Walter Kolar <sup>1</sup><sup>1</sup> Power Electronic Systems Laboratory, ETH Zurich, 8092 Zurich, Switzerland; kolar@lem.ee.ethz.ch<sup>2</sup> Levitronix GmbH, 8048 Zurich, Switzerland

\* Correspondence: bagaric@lem.ee.ethz.ch

**Abstract:** To enhance the fluid dynamic performance of bearingless cross-flow fans (CFFs), this paper presents a CFD-based optimisation of both rotor and static casing wall modifications. High-performance CFFs are essential in industrial applications such as highly specialised laser modules in the semiconductor industry. The goal for the investigated rotor modifications is to enhance the CFF's mechanical stiffness by integrating reinforcing shafts, which is expected to increase the limiting bending resonance frequency, thereby permitting higher rotational speeds. Additionally, the effects of these rotor modifications on the fluid dynamic performance are evaluated. For the casing wall modifications, the goal is to optimise design parameters to reduce losses. Optimised bearingless CFFs benefit semiconductor manufacturing by improving the gas circulation system within the laser module. Higher CFF performance is a key enabler for enhancing laser performance, increasing the scanning speed of lithography machines, and ultimately improving chip throughput. Several numerical simulations are conducted and validated using various commissioned prototypes, each measuring 600 mm in length and 60 mm in outer diameter. The results reveal that integrating a central shaft increases the rotational speed by up to 42%, from 5000 rpm to 7100 rpm, due to enhanced CFF stiffness. However, the loss in fluid flow amounts to 61% and outweighs the gain in rotational speed. Optimising the casing walls results in a 22% increase in maximum fluid flow reaching 1800 m<sup>3</sup>/h at 5000 rpm. It is demonstrated that the performance of bearingless CFFs can be enhanced by modifying the geometry of the casing walls, without requiring changes to the CFF rotor or bearingless motors.



**Citation:** Bagaric, I.; Steinert, D.; Nussbaumer, T.; Kolar, J.W. Computational Fluid Dynamics-Based Optimisation of High-Speed and High-Performance Bearingless Cross-Flow Fan Designs. *Machines* **2024**, *12*, 513. <https://doi.org/10.3390/machines12080513>

Received: 10 June 2024

Revised: 17 July 2024

Accepted: 27 July 2024

Published: 29 July 2024



**Copyright:** © 2024 by the authors. Licensee MDPI, Basel, Switzerland. This article is an open access article distributed under the terms and conditions of the Creative Commons Attribution (CC BY) license (<https://creativecommons.org/licenses/by/4.0/>).

**Keywords:** bearingless motors; cross-flow fan; fluid dynamics; computational fluid dynamics; performance; rotor dynamics

## 1. Introduction

Cross-flow fans (CFFs) are a type of fan turbomachinery that are characterised by their large length-to-diameter ratio and ability to generate a primarily uniform flow along their length at low rotational speeds and low noise emission. Therefore, they are predominantly employed in heating, ventilation, and air conditioning (HVAC) systems. However, the application scope of CFFs extends to industrial applications such as highly specialised laser modules in the semiconductor industry. These applications require high CFF performance to maintain consistent and high-quality laser output through the gas circulation system. In [1], the authors presented the bearingless CFF, which allows for wear- and friction-free CFF operation inside a hermetically sealed chamber with high-speed capability, supported by high drive power available on both rotor sides. To enhance the fluid dynamic performance of bearingless CFF's within a given, constrained installation space (as shown in Figure 1a), this paper conducts a Computational Fluid Dynamics (CFDs)-based design optimisation supported and verified by measurements. On the one hand, design measures are investigated to increase the CFF's mechanical strength through introducing stiffness increasing shafts. This shifts the critical bending resonance frequency, which currently

limits the maximum achievable rotational speed to a higher frequency, thus enabling stable CFF operation at increased rotational speeds. On the other hand, design changes of the CFF casing walls are evaluated to improve its fluid dynamic performance, particularly to reduce recirculation losses between the rotating blades and the static casing walls. The investigated design measures are depicted in Figure 1b,c.

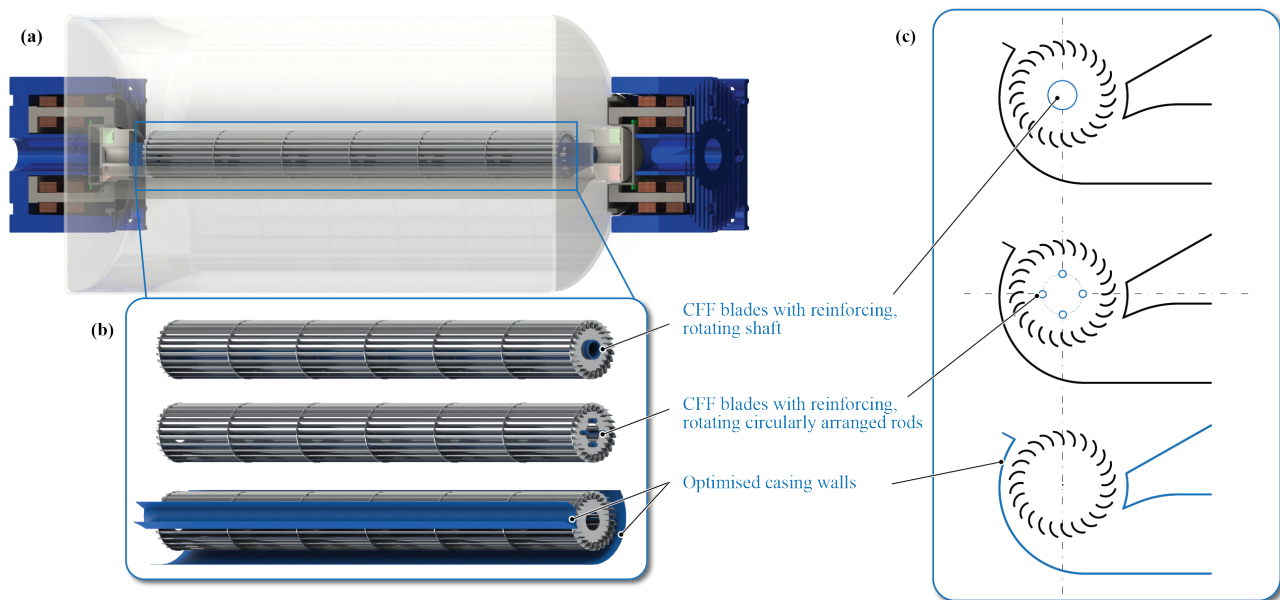


**Figure 1.** (a) Schematic view of the bearingless CFF system in a hermetically sealed laser chamber. (b) Investigated measures to increase the CFF's performance through additional mechanical elements (shaft and circularly arranged rods) to increase its mechanical strength and thereby its rotational speed and through optimisation of the casing walls. (c) Cross-sectional view of the CFDs-based performance analysis, highlighting the design adaptations under investigation, marked in blue.

In industrial applications such as deep ultraviolet (DUV) lithography systems, CFFs are part of the gas circulation system. DUV lithography systems use short-wavelength ultraviolet (UV) light, typically provided by an argon fluoride (ArF) or krypton fluoride (KrF) excimer laser, to project intricate patterns onto silicon wafers for the precise fabrication of semiconductor devices. CFFs, with their cylindrical shape and tangential flow direction, are compactly integrated within the limited space constraints of the excimer laser to uniformly circulate and cool the laser gas [2–4]. Increasing the CFF's performance can positively impact various aspects of laser performance, including cooling efficiency, gas circulation, flow stability and reliability, which contributes to achieving consistent and high-quality laser output. Hence, increasing the CFF's performance is a direct enabler for improving the excimer lasers's performance.

To increase the CFF's performance by increasing its rotational speed, the bending resonance frequency emerges as a critical factor, since CFFs typically consist of long, slender blades that are prone to bending vibrations. When the rotational speed approaches or exceeds the bending resonance frequency, it can lead to significant structural vibrations and potentially cause mechanical damage to the CFF blades. In [1], the authors provided an in-depth explanation of how the bending resonance frequency emerges as the speed and performance-limiting factor for the bearingless CFF. With the proposed bearingless motor technology, both the bearing and drive functionalities are integrated into a single motor unit, with a drive motor implemented on each side of the CFF rotor. This setup enables contactless levitation and rotation, with each motor independently controlling the bearing forces on its respective rotor side. The drive torque is generated by both motors, with a reference torque current passed from the primary to the secondary motor. Thus, each motor contributes half of the required drive torque, ensuring an even distribution of the

load. A detailed description of the operating principle can be found in [1]. It is emphasised that the magnetic bearing can only withstand forces and allow displacements to a limited extent. In [5], the authors proposed a method to shift the detrimental bending resonance frequency to higher frequencies through the design of a novel CFF rotor. The rotor features additional mechanical decoupling elements with low bending stiffness, allowing resonance frequencies to be surpassed without causing damage to the CFF blades and enabling rotor operation at a 40% higher rotational speed. Moreover, with magnetic bearings, it becomes feasible to implement complex control algorithms to actively control specific vibration modes. This offers the capability to dampen, bypass, or eliminate resonance frequencies, such as the bending resonance frequency. In the literature, different approaches have been investigated, typically for massive shafts and Jeffcott rotors. In [6], an optimum compensator control design method was proposed to obtain the minimum resonance peak of the rotor when passing the first bending critical speed. To operate a maglev motor above the bending critical speed, ref. [7] designed a  $\mu$ -synthesis controller and experimentally verified that the rotor passed through the first bending mode frequency. A  $\mu$ -synthesis controller was designed by [8] as well to achieve active damping of the rotor's bending mode and pass through its critical speed. Using a mixed PID control method based on mode separation, ref. [9] showed by simulation that the flexible rotor can pass the first bending critical speed.

This paper examines two additional methods for enhancing the CFF's performance that can be implemented alongside the previously mentioned damping techniques. From a fluid dynamical point of view, the CFF's non-axisymmetric flow profile is defined by the transverse double passage of the fluid through the rotating blades and the formation of an eccentric vortex within the impeller. There is not yet a general approach or analytical description to accurately model the aerodynamic features and loss mechanisms of CFFs nor to precisely predict their performance. Several different investigations about CFFs were conducted using analytical modelling, numerical simulation, and experimental data [10–13]. To analytically determine the CFF performance curves for a given geometry, refs. [14–16] used the mean streamline analysis with empirical data. Numerous numerical and experimental studies have been conducted to analyse the influence of the CFF blades' [17–19] and casing walls geometry [20–23] on the CFF performance. A particular focus lies in visualising the complex flow patterns by means of CFDs and analysing the velocity vectors and pressure gradients to draw conclusions about CFF performance, efficiency, and loss mechanisms [24–27]. In [28], Stereo Particle Image Velocimetry (SPIV) was presented as an experimental flow visualisation technique to examine the influence of CFF casing geometries. In a recently published review paper on the performance and efficiency of CFFs [29], it was concluded that optimising and enhancing their performance remains a challenging task. To boost the CFF's efficiency, it is crucial to improve its structural characteristics, aerodynamic properties, and acoustic behaviour.

Compared to existing approaches in CFF analysis, this study integrates fluid dynamics, rotor dynamics, and various aspects of the mechatronic system through experimental measurements. Particularly, increasing the performance of bearingless CFFs presents several challenges concerning fluid dynamics, rotor dynamics (mechanical strength and rotor vibrations), and the influence on the magnetic bearing. The fluid forces can lead to displacements of the magnetically levitated rotor, requiring measures to prevent collisions with the static casing walls by maintaining a certain safety distance. The goal of this paper is to optimise the CFF performance in terms of output pressure and flow while considering the different effects on the bearingless motor system.

The paper is organised as follows: Section 2 presents the methods used for the CFF rotor and casing wall optimisation, including the fundamental aerodynamics, implemented CFD model, simulated modal analysis, and measurement setup. Section 3 reveals and discusses the results for the different rotor and static casing walls design modifications. Section 4 summarises the main conclusions.

## 2. Methods for CFF Analysis

### 2.1. Fundamental Aerodynamics

This section explains the operating principle of CFFs from a fluid dynamical point of view, particularly to underline the loss mechanisms associated with the characteristic eccentric vortex. The goal of this analysis is to explore methods for enhancing the performance of the CFF by modifying both the rotor and static casing walls within given space constraints. Regarding the rotor modifications, the primary focus is on increasing mechanical stiffness through the integration of reinforcing shafts and evaluating their impact on fluid dynamic performance. In terms of the static casing walls, the emphasis is on optimising the eccentric vortex region to reduce recirculation losses.

Generally, the energy increase of a fan turbomachinery represents the change in energy of the fluid passing through the fan from the inlet to the outlet side, i.e., from the suction to the discharge region. This energy increase is typically defined in terms of total pressure  $\Delta p_{th\infty}$  and can be expressed as the sum of both the static and dynamic pressure components as the first form of Euler's fluid machine equation:

$$\Delta p_{th\infty} = \frac{\rho}{2} \left[ \overbrace{(c_2^2 - c_1^2)}^{\text{dynamic}} + \overbrace{(w_1^2 - w_2^2) + (u_2^2 - u_1^2)}^{\text{static}} \right], \quad (1)$$

where  $c$  is the absolute,  $u$  is the circumferential,  $w$  is the relative velocity, and  $\rho$  is the density. The geometric sum of the circumferential and relative velocity gives the absolute velocity, which defines the second form of Euler's fluid machine equation as

$$\Delta p_{th\infty} = \rho(u_2 \cdot c_{u2} - u_1 \cdot c_{u1}). \quad (2)$$

For CFFs, the flow field is predominately two-dimensional, i.e., perpendicular to the impeller axis. It is described by the fluid entering the forward curved blades tangentially on the suction side, passing through the interior part of the impeller, and then exiting the blades tangentially on the discharge side. Hence, the rotating blades are passed twice by the fluid, and an eccentric vortex is formed within the impeller. The eccentric vortex is a characteristic flow pattern inherent to the design and operation of CFFs.

To explain the fundamental kinematics and energy transfer processes for CFFs, Figure 2 is used. It is based on [14], who describe in detail the throughflow and loss characteristics of the CFF by the mean streamline analysis. The analysis has the underlying assumption that the flow within the fan can be divided into three regions (depicted as work region A, paddle region B, and eccentric vortex region C in Figure 2a) and can be analysed independently. However, the flow is strongly influenced by the operating conditions and the fan geometry, which can be difficult to parameterise.

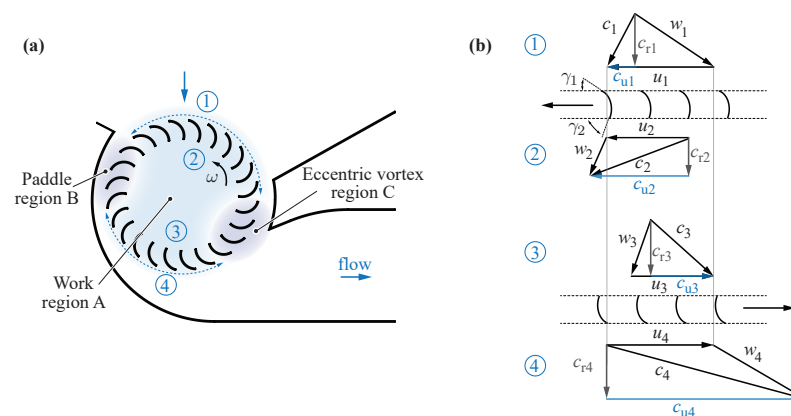


**Figure 2.** (a) Flow regions of the CFF divided into the work region A, paddle region B, and eccentric vortex region C adapted from [14]. (b) Velocity triangles in the two stages of the CFF.

The principal throughflow of the impeller is represented by region A, where the majority of the beneficial work is conducted, and is described by the velocity triangles in Figure 2b. Using Equation (2), the ideal total pressure increase across the CFF impeller  $\Delta p_{th\infty,14}$  is given by the sum of the first and second stage total pressure increase as

$$\Delta p_{th\infty,14} = \rho \left( (u_2 c_{u2} - u_1 c_{u1}) + (u_4 c_{u4} - u_3 c_{u3}) \right). \quad (3)$$

The actual total pressure increase  $\Delta p_{tot,14}$  is then given by

$$\Delta p_{tot,14} = \Delta p_{th\infty,14} - \Delta p_{loss} \quad (4)$$

where the pressure losses  $\Delta p_{loss}$  are an unknown parameter consisting of several different loss mechanisms. In [15], the most important loss models of the mean streamline analysis are summarised as skin friction, incidence expansion, enlargement, and recirculation losses. As explained in [14], the CFF blades in region B act essentially like a paddle wheel; hence, the energy transfer is comparatively low and inefficient. Region C represents the eccentric vortex, which consists of the recirculating flow and is primarily responsible for energy dissipation and the shaping of region A.

From the CFFs operating principle described above, it becomes clear that introducing interior obstructions within work region A, such as mechanically reinforcing shafts, causes flow disturbances and additional losses. However, these stiffness-increasing measures have a significant impact on the CFF's vibration behaviour, especially its bending resonance frequency.

Various diameters of reinforcing shafts have been studied, as depicted in Figure 3a for a single central shaft and in Figure 3b for circularly arranged rods. Regarding the casing wall optimisation, its key geometric parameters are presented in Figure 3c, and different variations have been investigated.

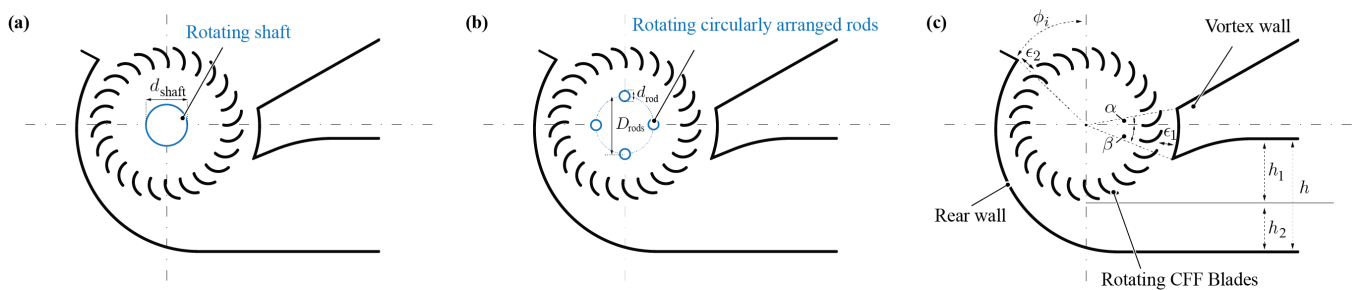


**Figure 3.** CFFs for the CFDs-based performance analysis (a) with reinforcing rotating shafts, (b) with reinforcing circularly arranged rods, and (c) parametrisation of the static casing walls, including the rear and vortex wall.

## 2.2. Computational Fluid Dynamics

For the CFDs analysis, planar 2D simulations were conducted, as the flow profile of the CFF remains predominantly uniform along its length. The numerical model utilised has been presented by the authors in [1]. The transient simulation model has been developed with air under ambient pressure and modelled as incompressible, since the expected Mach numbers are below 0.3 (subsonic). Furthermore, the sliding mesh method was employed for the calculations, with the  $k-\omega$  SST model used for turbulence modelling. A detailed description, including a convergence study involving mesh and time step parameters for the transient CFF CFDs simulation can be found in [1], which led to a robust model with optimised mesh and time step settings.

Figure 4 illustrates the velocity and pressure profiles resulting from the CFD simulation for the initial CFF geometry at 5500 rpm and  $1633 \text{ m}^3/\text{h}$  (high-flow point). The velocity vectors provide a visual representation of the key fluid dynamic features, highlighting the

inflow and outflow regions, as well as the non-axisymmetric flow profile. Additionally, the pressure profile vividly illustrates the presence of the eccentric vortex.

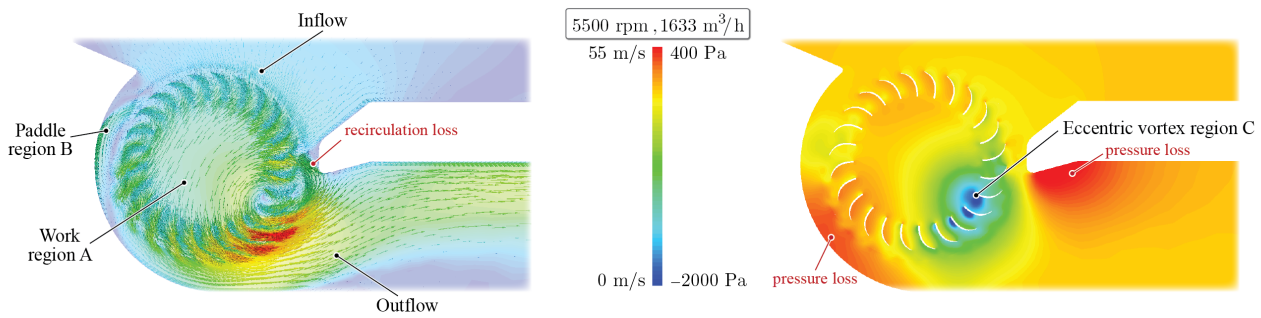


**Figure 4.** CFDs-simulated velocity (left) and pressure (right) profiles for the initial CFF geometry for a stable, high-flow operating point at 5500 rpm.

For the forthcoming comparisons and performance evaluations, the dimensionless flow  $\varphi_{\text{CFF}}$  and pressure  $\psi_{\text{stat,CFF}}$  coefficients are evaluated from the simulated physical flow  $Q$  and pressure values  $\Delta p_{\text{stat}}$  according to

$$\varphi_{\text{CFF}} = \frac{Q}{u \cdot d_{\text{CFF}} \cdot L_{\text{CFF}}} \quad (5)$$

where  $d_{\text{CFF}}$  and  $L_{\text{CFF}}$  correspond to the CFF blades' diameter and length, and  $u$  corresponds to the circumferential velocity

$$u = \pi \cdot d_{\text{CFF}} \cdot n \quad (6)$$

with  $n$  being the CFF's rotational speed and

$$\psi_{\text{stat,CFF}} = \frac{\Delta p_{\text{stat}}}{\rho_{\text{air}}/2 \cdot u^2} \quad (7)$$

where  $\rho_{\text{air}}$  is the density of air. Introducing shafts within the CFF impeller changes its bending resonance frequency and can increase the rotational speed at which it can be operated. The dimensionless pressure and flow coefficients allow us to extrapolate the physical pressure and flow for operating points at different rotational speeds according to

$$Q^* = \frac{n^*}{n} \cdot Q \quad (8)$$

and

$$\Delta p_{\text{stat}}^* = \left(\frac{n^*}{n}\right)^2 \cdot \Delta p_{\text{stat}} \quad (9)$$

with  $Q^*$  representing the extrapolated flow and  $\Delta p_{\text{stat}}^*$  representing the extrapolated pressure derived from the CFDs results at different rotational speeds of  $n^*$ .

The CFDs simulation was conducted for several high-flow operating points and compared to measured data points in Figure 5. To derive the flow rate from the 2D simulation, the inlet velocity was multiplied by the cross-sectional area defined by the inlet channel's height and width. The dotted lines of the simulated curve mark the pressure fluctuation in the CFD simulation during the final turn, indicating convergence and a stable eccentric vortex region, i.e., no pressure pulsations. As described in [1], an operation point converges after approximately six turns, while one turn (a  $360^\circ$  rotation of the fan blades) corresponds to 66.67 numerical time steps. It can be seen that the simulated and measured data points agree very well.

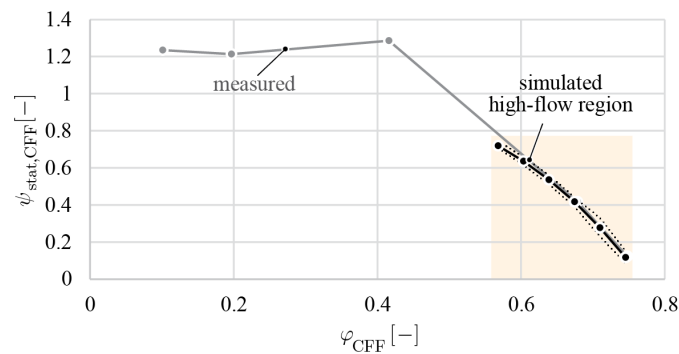


**Figure 5.** Dimensionless pressure–flow curves of initial CFF geometry measured on a test bench presented in [1] and simulated in the high-flow region. The pressure  $\psi_{stat,CFF}$  and flow  $\varphi_{CFF}$  coefficients are calculated according to Equations (5) and (7). The dotted lines mark the pressure fluctuation observed in the CFD simulation during the final turn, indicating convergence and a stable eccentric vortex region.

For this study, the simulated operating points of the different design adaptations were focused on the high-flow regime. At low-flow operating points, the implemented incompressible CFDs model (justified with the expected subsonic speeds of Mach numbers below 0.3) predicted strong pressure fluctuations, which inadequately represent the physical conditions. In [30], it was observed that as the flow decreases, the eccentric vortex region C expands. Consequently, it is more challenging for the inlet flow to efficiently penetrate work region A of the CFF, which exacerbates the non-uniformity and amplifies the pressure pulsations within region C. In [31], it was concluded as well that the dominant frequency responsible for the velocity and pressure fluctuations in the CFF is mainly generated due to the unsteadiness of the eccentric vortex. The flow in the low-flow region was described as strongly unsteady, unstable, and three-dimensional in [16]. Therefore, the following simulations focus on numerically stable, high-flow operating points, aligning with the typical CFF application for generating uniform flow patterns along their length.

To quantitatively compare the modified and initial CFF design, the simulated operating points at the same dimensionless static inlet pressure  $\psi_{stat,CFF}$  were evaluated to determine the change in fluid flow as  $\Delta\varphi_{CFF,max}$ .

### 2.3. Simulated Modal Analysis

A modal analysis was performed on the CFF rotor modifications with various shafts to estimate the system's first bending resonance frequency to draw conclusions about the maximum achievable rotational speed. It is described in more detail in [1]. This theoretical assessment of different shaft sizes and arrangements assists in determining which prototypes to commission.

### 2.4. Measurement Setup

The CFD simulations and experimental measurements were conducted for a CFF with  $L_{CFF} = 600$  mm and  $d_{CFF} = 60$  mm. The pressure–flow measurements were performed with air under ambient pressure on a test rig presented in detail in [1]. It consists of an inlet ventilation duct equipped with a variable inlet grid for setting different operating points, along with a pressure and a flow sensor. Characteristic pressure–flow curves can be recorded for various design modifications.

For the rotor dynamic measurements, the displacements of the rotor magnet within the magnetic bearing were evaluated using built-in sensors in the bearingless motor. The bending resonance frequency was identified by the rapid increase in radial displacements as it was approached.

### 3. Results and Discussion

This section presents the results of the CFF analysis for different rotor and stator modifications. The quantitative results of the CFD analysis of the modified CFF rotor with reinforcing shafts (Figure 3a) and circularly arranged rods (Figure 3b) are summarised in Table 1 and of the modified CFF static casing walls (Figure 3c) in Table 2. It is shown that rotor modifications with shafts do not lead to an increase in CFF performance. Specifically, the shafts, which do not contain blades, were used as the modification object to investigate their potential rotor stiffening effect. Optimising the casing wall resulted in a performance improvement of up to 22%. A detailed analysis and discussion of the results is presented next.

**Table 1.** CFDs results for the modified CFF rotor evaluated as change in fluid flow  $\Delta\varphi_{\text{CFF,max}}$  compared to initial CFF geometry from Figures 4 and 5.

	Rotor Modifications	Design Properties	$\Delta\varphi_{\text{CFF,max}}$ (%)
(a1)	central shaft	$d_{\text{shaft}} = 12 \text{ mm}$	−44
(a2)	central shaft	$d_{\text{shaft}} = 15 \text{ mm}$	−51
(a3)	central shaft	$d_{\text{shaft}} = 20 \text{ mm}$	−61
(b1)	circularly arranged rods	$d_{\text{rod}} = 5 \text{ mm}, D_{\text{rods}} = 20 \text{ mm}$	−38
(b2)	circularly arranged rods	$d_{\text{rod}} = 5 \text{ mm}, D_{\text{rods}} = 30 \text{ mm}$	−29

**Table 2.** CFD results for modified CFF static casing wall evaluated as change in fluid flow  $\Delta\varphi_{\text{CFF,max}}$  compared to initial CFF geometry from Figures 4 and 5.

	Static Casing Wall Modifications	Design Properties	$\Delta\varphi_{\text{CFF,max}}$ (%)
(c1)	increased inlet angle $\phi_i$	$h = 43.5 \text{ mm}, h_2 = 13.5 \text{ mm}, e_2 = 8.6 \text{ mm}, \phi_i = 65^\circ$	+0
(c2)	rear wall downward shift	$h = 48.5 \text{ mm}, h_2 = 18.5 \text{ mm}, e_2 = 5 \text{ mm}, \beta = 7.2^\circ$	+10
(c3)	rear and vortex wall downward shift	$h = 43.5 \text{ mm}, h_2 = 18.5 \text{ mm}, e_2 = 5 \text{ mm}, \beta = 14.9^\circ$	+15
(c4)	optimised outlet side	$h = 47.8 \text{ mm}, h_1 = 29 \text{ mm}, e_2 = 5 \text{ mm}, \beta = 11.7^\circ$	+22

#### 3.1. Rotor Modifications

##### 3.1.1. Reinforcing Central Shaft

For different sizes of reinforcing central shafts, denoted as designs (a1), (a2), and (a3) in Table 1, the pressure–flow performance of the CFF significantly decreased, as depicted in Figure 6a. The evaluated change in dimensionless flow  $\Delta\varphi_{\text{CFF,max}}$  corresponds to −44%, −51% and −61% for shafts with diameter  $d_{\text{shaft}} = 12 \text{ mm}$ ,  $d_{\text{shaft}} = 15 \text{ mm}$ , and  $d_{\text{shaft}} = 20 \text{ mm}$ . The simulations for the reinforcing shafts with diameters of 12 mm and 20 mm were additionally validated with pressure–flow measurements on the test bench.

The velocity and pressure profiles for a shaft diameter of 12 mm are visualised in Figure 7. It can be seen that the presence of the shaft obstructs the flow field within the impeller, causing localised flow blockage and disrupting the formation of the eccentric vortex. Consequently, losses occurred, which increased with the shaft diameter.

Furthermore, five distinct CFF prototypes featuring central reinforcing shafts were rotor dynamically analysed. Various configurations of hollow and solid shafts, made from either stainless steel or aluminium, were tested. Their respective bending resonance frequencies were determined through modal simulation and, for the commissioned prototypes, tested on the test bench, as listed in Table 3. For all simulated CFF rotors, the simulation model overestimated the mechanical stiffness and consequently the first bending resonance frequency. This discrepancy arises from the multi-body nature of the prototype and the imperfect bonding between individual components, whereas in the simulation the CFF rotor was assumed as one single solid body. For a stainless steel shaft with a diameter of 12 mm, the critical rotational speed  $n_{\text{crit,meas}}$  was measured at 5100 rpm. This speed is lower compared to the initial CFF critical rotational speed of 5800 rpm, thus indicating that the overall increase in mass outweighs the increase in mechanical bending stiffness. The 15 mm hollow stainless steel shaft rose  $n_{\text{crit,meas}}$  to 6300 rpm. Additionally, the 20 mm hollow

aluminium and stainless steel shafts increased the  $n_{crit,meas}$  to 6800 rpm and 8200 rpm, respectively.

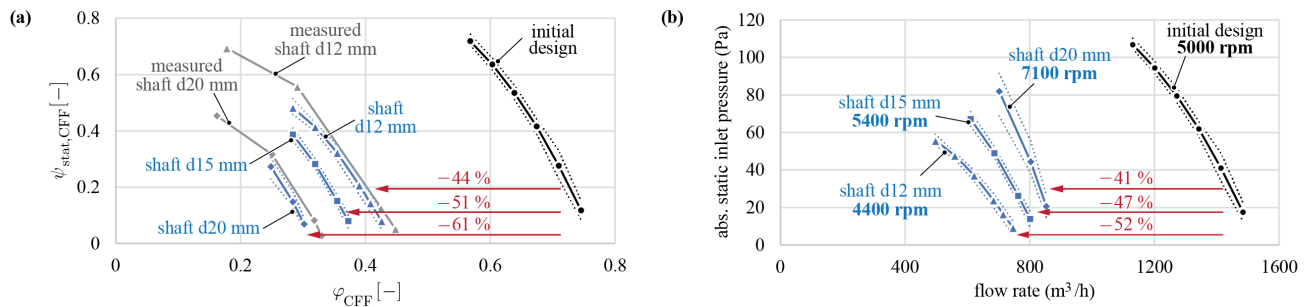


**Figure 6.** (a) Dimensionless pressure–flow curves for the CFF rotor with reinforcing shafts simulated for shaft diameters  $d_{shaft}$  of 12 mm, 15 mm, and 20 mm. The CFDs results were validated for  $d_{shaft}$  of 12 mm and 20 mm with measurements on the test bench. (b) Extrapolated pressure–flow curves according to Equations (8) and (9) to the maximal possible rotational speed  $n^*$ , where  $n^*$  was determined by the resonance frequencies from Table 3 with a safety margin of ca. 14% as determined in [5].

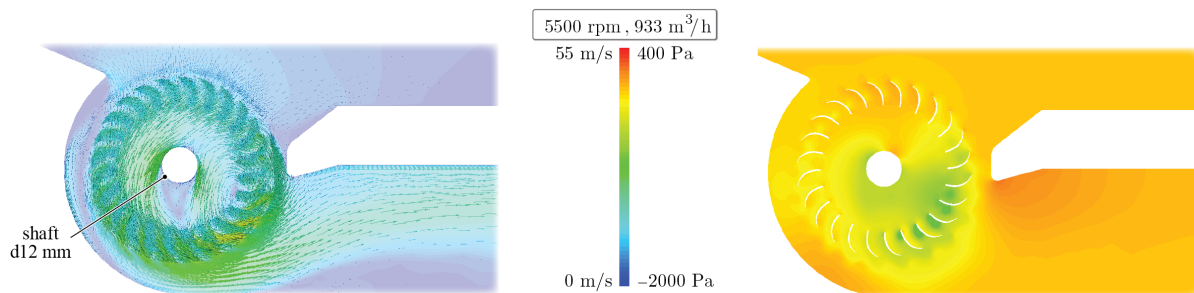


**Figure 7.** CFDs-simulated velocity (left) and pressure (right) profiles for the modified CFF rotor with central shaft with a diameter of 12 mm for a stable, high-flow operating point at 5500 rpm.

With a safety margin of approximately 14% from the critical resonance frequency as determined in [5], the dimensionless pressure–flow curves depicted in Figure 6a were extrapolated for the initial design to 5000 rpm, for a shaft diameter  $d_{shaft} = 12$  mm to 4400 rpm, for  $d_{shaft} = 15$  mm to 5400 rpm, and for  $d_{shaft} = 20$  mm to 7100 rpm according to Equations (8) and (9).

It can be concluded that even with the highest rotational speed increase of 42% due to the enhanced stiffness of the CFF with  $d_{shaft} = 20$  mm, the loss in fluid dynamic performance of  $-61\%$  outweighs the gain in rotational speed resulting in an overall performance decrease of  $-41\%$ , as shown in Figure 6b.

**Table 3.** Simulated and measured critical rotational speeds of CFF blades with reinforcing shafts.

$d_{shaft,out}/d_{shaft,in}$ (mm)/(mm)	Material (-)	$n_{bend,sim}$ (rpm)	$n_{bend,meas}$ (rpm)
-	aluminium	7360	5800
12/0	stainless steel	7290	5100
15/11	stainless steel	8800	6300
20/14	aluminium	10,850	6800
20/16	stainless steel	11,310	8200

### 3.1.2. Reinforcing Circularly Arranged Rods

The CFDs results of the dimensionless pressure–flow curves for CFFs with reinforcing circularly arranged rods are shown in Figure 8. Similarly to the designs with central

shafts, the performance decreased due to flow obstructions. The evaluated change in dimensionless flow  $\Delta\varphi_{\text{CFF,max}}$  for rods of  $d_{\text{rod}} = 5 \text{ mm}$  corresponds to  $-29\%$  and  $-38\%$  arranged at diameter  $D_{\text{rods}} = 30 \text{ mm}$  and  $D_{\text{rods}} = 20 \text{ mm}$ , respectively. Placing the rods at a larger diameter disrupted the formation of the eccentric vortex less.

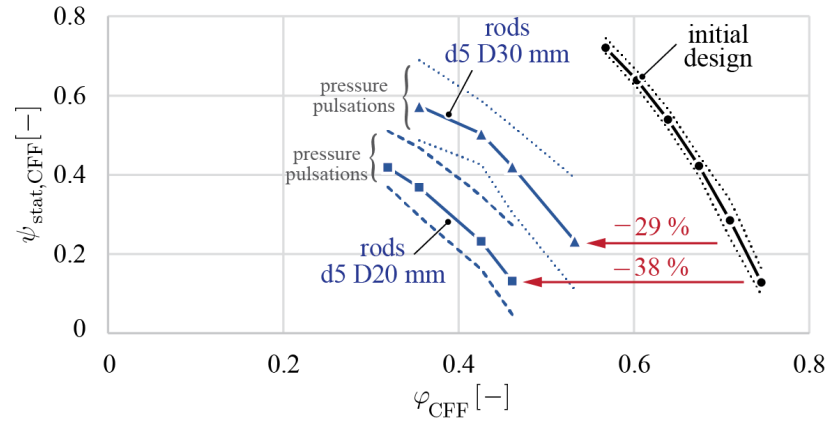


**Figure 8.** Dimensionless pressure–flow curves for the CFF rotor with reinforcing circularly arranged rods simulated for a rod diameter  $d_{\text{rod}} = 5 \text{ mm}$  and circle diameters  $D_{\text{rods}} = 20 \text{ mm}$  and  $D_{\text{rods}} = 30 \text{ mm}$ , respectively.

However, the rods interact with the eccentric vortex generated by the impeller blades, inducing significant pressure pulsations, as they penetrate it at a frequency four times the rotational frequency of the rotor. Consequently, the stability and uniformity of the flow distribution deteriorated. The velocity and pressure profiles for  $D_{\text{rods}} = 30 \text{ mm}$  are visualised in Figure 9.

The simulated bending resonance frequencies are listed in Table 4. The increase in mechanical stiffness and hence the shift to higher bending resonance frequency was below 3%. Therefore, no prototypes have been commissioned.

In summary, neither the reinforcing central shafts nor the circularly arranged rods led to an increase in CFF performance.

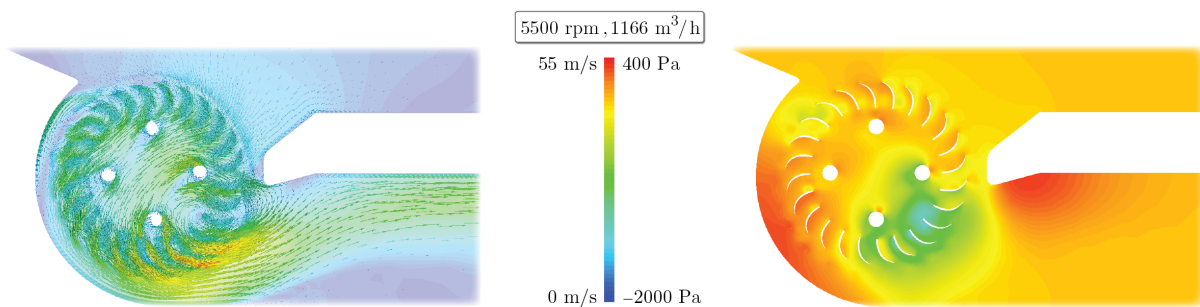


**Figure 9.** CFDs-simulated velocity (left) and pressure (right) profiles for the modified CFF rotor with circularly arranged rods ( $d_{\text{rod}} = 5 \text{ mm}$  and  $D_{\text{rods}} = 30 \text{ mm}$ ) for a stable, high-flow operating point at 5500 rpm.

**Table 4.** Simulated critical rotational speeds of CFF blades with reinforcing circularly arranged rods.

$d_{\text{rod}}/D_{\text{rods}}$ (mm)/(mm)	Material (-)	$n_{\text{bend,sim}}$ (rpm)	$n_{\text{bend,meas}}$ (rpm)
-	aluminium	7360	5800
5/20	stainless steel	7260	—
5/30	stainless steel	7530	—

### 3.2. Static Casing Walls Modifications

For the CFD analysis of modifications to the static casing walls, the primary focus lies on the vortex wall, as CFFs are particularly prone to creating recirculation zones in this area. The CFD simulations were conducted for minor geometry changes, allowing us to track the specific effects of each modification, thus providing a clear understanding of their impact on the overall performance. It has to be ensured that any changes are comprehensible and can be implemented and validated through physical testing. Furthermore, the distance between the fan blades and the vortex wall, defined as  $\epsilon_1$  in Figure 3c, was kept constant to maintain the necessary safety distance required due to the use of magnetic bearings.

The following modifications include an increased inlet angle, a downward shift of the rear wall, and adaptations of the vortex wall inlet and outlet side.

#### 3.2.1. Increased Inlet Angle $\phi_i$

To analyse the influence of paddle region B on fan performance, the inlet angle  $\phi_i$  of the initial design was significantly increased from  $40^\circ$  to  $65^\circ$ .

The dimensionless pressure–flow curves resulting from the CFDs analysis in the high-flow region are shown in Figure 10. Comparing the initial design to the modified, it is observed that the dimensionless flow  $\Delta\varphi_{\text{CFF,max}}$  remained almost unaffected by this change. This indicates that the inlet modification of  $\phi_i$  has a negligible impact on performance.

Comparing the velocity and pressure profiles from the initial design shown in Figure 4 to those of the design with changed inlet angle in Figure 11 reveals that the size of paddle region B was reduced, while work region A remained largely unchanged. This suggests that the impact of the rear wall inlet side modification on fan performance is negligible.

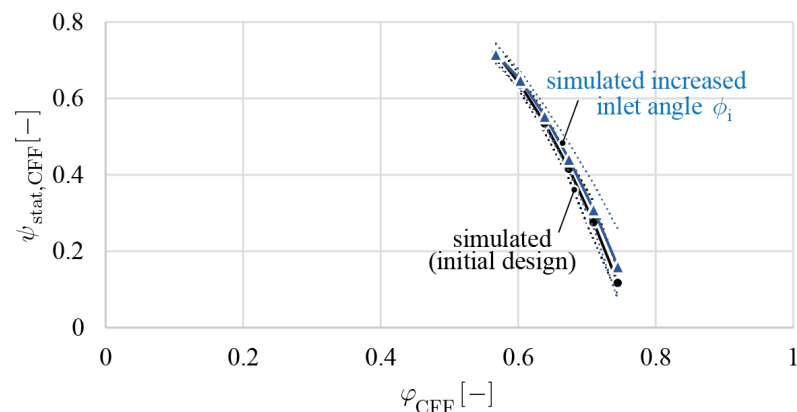


**Figure 10.** Simulated dimensionless pressure–flow curve for the CFF with static casing wall with increased inlet angle  $\phi_i$  from  $40^\circ$  to  $65^\circ$ . Compared to the initial design, the dimensionless flow  $\Delta\varphi_{\text{CFF,max}}$  remained almost unaffected by this change, indicating that  $\phi_i$  has minimal influence on performance.

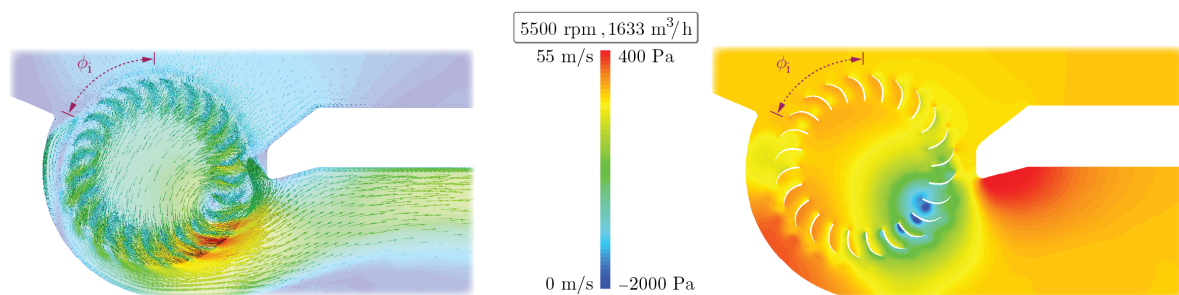


**Figure 11.** CFDs-simulated velocity (left) and pressure (right) profiles for the CFF with increased inlet angle  $\phi_i$  for a stable, high-flow operating point at 5500 rpm. This modification reduced the size of paddle region B, while work region A remained largely unaffected; hence, there is minimal impact on fan performance.

### 3.2.2. Rear Wall Shift

This modification involves a downward shift of the rear wall. The adjustment changes the outlet parameters  $h$  and  $h_2$ , as well as the inlet distance from the rotor to the rear wall  $\epsilon_2$ , as defined in Figure 3c, while the geometry of the vortex wall remains unchanged.

The CFDs results of the dimensionless pressure–flow curves are shown in Figure 12, indicating a 10% increase in the maximum dimensionless flow  $\Delta\varphi_{\text{CFE,max}}$ . Comparing the pressure profiles between the resulting design shown in Figure 13 and the original configuration depicted in Figure 4, a reduction in the high-pressure zone at the outlet side of work region A was achieved, leading to less pressure losses.

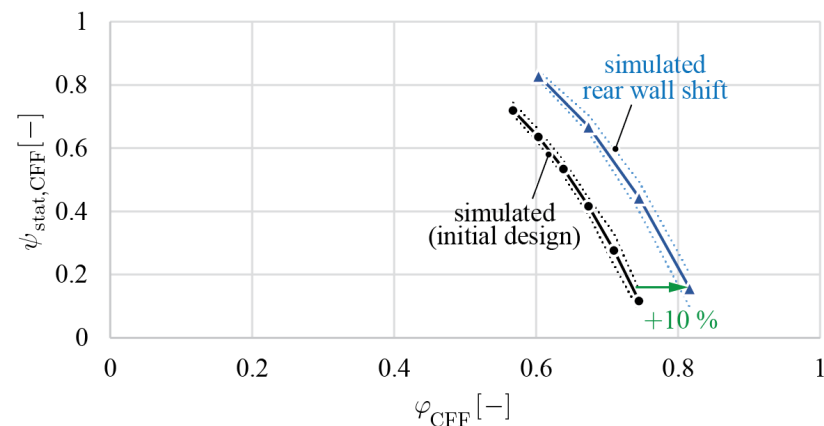


**Figure 12.** Simulated dimensionless pressure–flow curve for the CFF with static casing wall modifications featuring a 5 mm downward shift of the rear wall. Compared to the initial design, the maximum dimensionless flow  $\Delta\varphi_{\text{CFE,max}}$  increased by 10%.

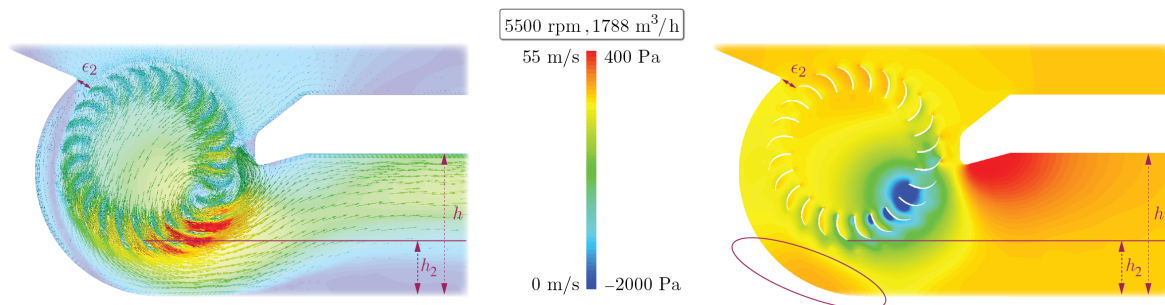


**Figure 13.** CFDs-simulated velocity (left) and pressure (right) profiles for the CFF with the rear wall shifted downward by 5 mm for a stable, with a high-flow operating point at 5500 rpm. The changes in outlet parameters  $h$ ,  $h_2$ , and the inlet distance from the rotor to the rear wall  $\epsilon_2$ , as defined in Figure 4, are marked, while the geometry of the vortex wall remained unchanged. Compared to the initial design in Figure 4, the high-pressure zone at the outlet side of work region A is reduced, leading to less pressure losses.

### 3.2.3. Rear and Vortex Wall Shift

In addition to the downward shift of the rear wall, the vortex wall was also shifted downward, altering the vortex wall inlet and outlet angles  $\alpha$  and  $\beta$ , respectively. The new design was simulated for several high-flow operating points, and the resulting dimensionless pressure–flow curve is shown in Figure 14. Compared to the initial design, this modification enhanced the dimensionless flow  $\Delta\varphi_{\text{CFE,max}}$  by 15%.

This casing wall modification has been commissioned and tested on the test bench, and the resulting dimensionless curve is plotted in Figure 14. The casing wall adaptation validates the CFDs simulation results very well in the high-flow region. Additionally, it can be seen from the measurements (grey), that these changes did not effect the pressure  $\psi_{\text{stat,CFE}}$  in the low-flow region.

The simulated velocity and pressure profiles for a stable, high-flow operating point at 5500 rpm are illustrated in Figure 15. The downward shift of the vortex wall decreased its inlet angle  $\alpha$  and increases its outlet angle  $\beta$ . When comparing the resulting pressure profile to the initial design shown in Figure 4, a lower eccentric vortex pressure is evident (indicated by dark blue scaling). This reduction in eccentric vortex pressure indicates that the airflow through the fan is more streamlined and encounters less resistance, resulting in improved performance in the high-flow region.

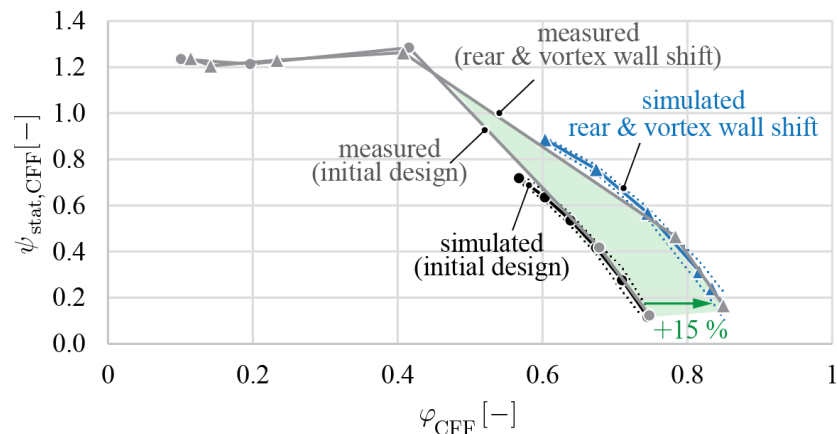


**Figure 14.** Dimensionless pressure–flow curve for the CFF with static casing wall modifications featuring a 5 mm downward shift of the rear and vortex walls. The curves were simulated in the high-flow region and measured on the test bench. Compared to the initial design, the maximum dimensionless flow  $\Delta\varphi_{\text{CFF,max}}$  increased by 15%. The green area highlights the newly measured performance gains.

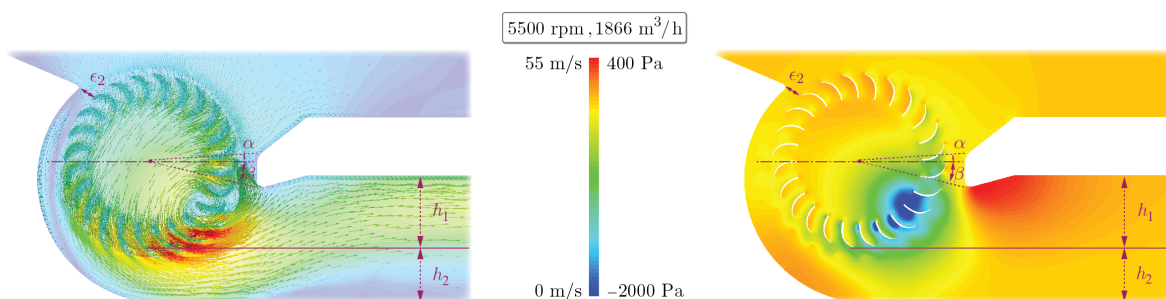


**Figure 15.** CFDs-simulated velocity (left) and pressure (right) profiles for the CFF with the rear and vortex wall shifted downward by 5 mm for a stable, high-flow operating point at 5500 rpm. The changes in outlet parameters  $h_1$ ,  $h_2$ , and the vortex wall angles  $\alpha$  and  $\beta$  are marked. Compared to the initial design shown in Figure 4, the pressure profile reveals a lower eccentric vortex pressure (dark blue scaling). This indicates a more streamlined airflow with reduced resistance through the fan, enhancing the fan performance in the high-flow region.

### 3.2.4. Adaptations of Outlet Side

Furthermore, the vortex wall outlet side was modified by adjusting the outlet height  $h_1$  and vortex wall outlet angle  $\beta$ . Four parameter sets were simulated at  $\varphi_{\text{CFF}} = 0.85$  (high flow), and the resulting dimensionless pressure  $\psi_{\text{stat,CFF}}$  was evaluated, as shown in Figure 16a. The most optimal configuration was identified with  $h_1 = 29$  mm and  $\beta = 11.8^\circ$ . Several additional points were simulated, as depicted in Figure 16b. Testing the new positioning of the vortex wall outlet on the test bench resulted in an increase of  $\Delta\varphi_{\text{CFF,max}}$  by 22%.

The simulated velocity and pressure profiles are shown in Figure 17. It can be concluded that varying  $h_1$  and  $\beta$  results in a tradeoff between the outlet resistance and recirculation. Increasing  $h_1$  resulted in a larger outlet, which thus reduced the resistance

encountered by the air as it leaves the CFF impeller blades (outlet side of work region A). However, this modification decreased  $\beta$ , allowing more recirculation in the eccentric vortex region C.

In summary, the static casing wall modifications were shown to enhance the CFF’s performance, achieving a maximum flow increase up to 22%.

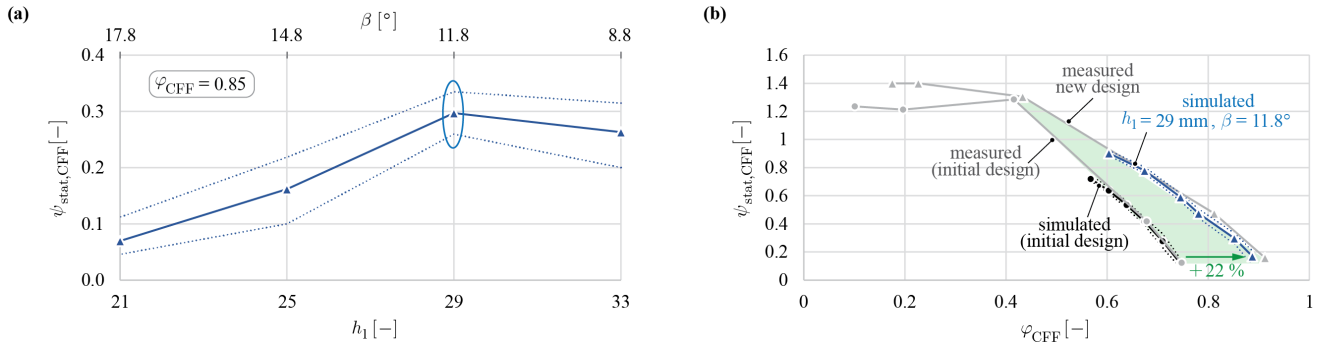


**Figure 16.** (a) Simulated dimensionless pressure  $\psi_{stat,CFF}$  for a high-flow operating point with  $\varphi_{CFF} = 0.85$  was analysed for different vortex wall outlet geometries, including variations in the vortex wall outlet height  $h_1$  and vortex wall outlet angle  $\beta$ . The configuration with  $h_1 = 29$  mm, and  $\beta = 11.8^\circ$  has been identified as optimal. (b) Dimensionless pressure–flow curve for the CFF with  $h_1 = 29$  mm and  $\beta = 11.8^\circ$ . The curves are simulated in the high-flow region and measured on the test bench. Compared to the initial design, the maximum dimensionless flow  $\Delta\varphi_{CFF,max}$  increased by 22%. The green area highlights the newly measured performance gains.

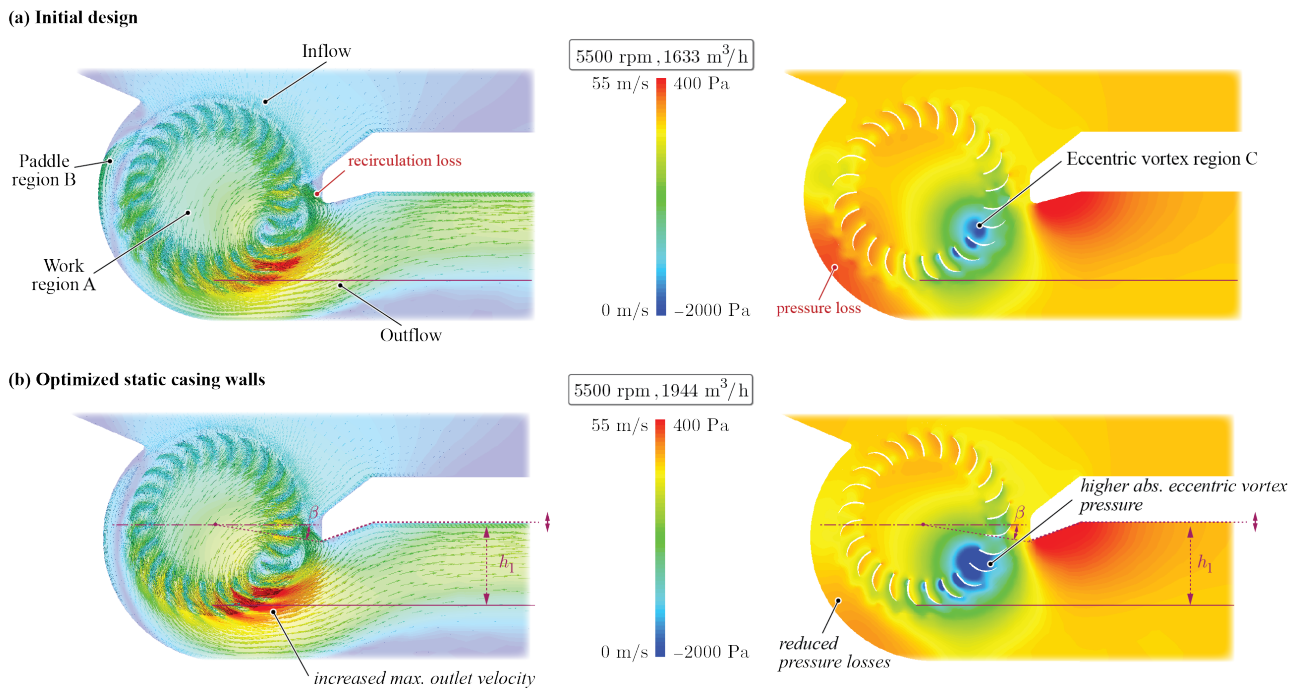


**Figure 17.** (a) Initial design from Figure 4 for the final comparison. (b) CFDs-simulated velocity (left) and pressure (right) profiles for the CFF with  $h_1 = 29$  mm and  $\beta = 11.8^\circ$  for a stable, high-flow operating point at 5500 rpm. An optimum was found between outlet resistance and recirculation.

#### 4. Conclusions

This study conducted a CFDs-based optimisation of measures to enhance the performance of bearingless CFFs, which is particularly important for certain industrial applications in the semiconductor industry. Modifications of the CFF rotor and static casing walls were investigated. Various prototypes were derived from the simulation results, which were then commissioned and tested.

It is concluded that to enhance CFF performance, the principal throughflow within the CFF impeller must remain unobstructed for fluid flow, and the eccentric vortex region must be stabilised through careful design of the vortex wall, while the paddle region (located on the fluid inlet side of the rear wall) is largely irrelevant for CFF performance.

Regarding the rotor modifications, introducing different dimensions of central shafts and circularly arranged rods as rotor stiffening methods within the CFF impeller impacts both the rotor dynamic and fluid dynamic performance. Specifically, a stainless steel shaft with a diameter of 20 mm shifts the critical bending resonance frequency of the CFF blades 42% higher. However, CFD simulations and experimental measurements showed that the flow dropped by 61%. The results indicate that while the reinforced CFF rotors achieved a higher rotational speed, this came at a significant cost to the fluid dynamic performance. Specifically, the increase in rotational speed did not compensate for the substantial reduction in fluid flow for all tested reinforced CFF rotors. This trade-off highlights the complexity of optimising both the mechanical and fluid dynamic aspects of the CFF rotor. The CFD investigation of circularly arranged rods additionally revealed that the rods induce significant, undesired pressure pulsations within the eccentric vortex. These pulsations lead to unstable flow patterns, which are not desired for their application in gas circulation systems of excimer lasers.

Regarding the casing wall modifications, the CFF performance is highly sensitive to changes in geometric parameters, particularly the vortex wall, as the casing walls directly influence the airflow path through the fan. A successful simulated and measured performance increase of up to 22% was achieved.

In summary, the paper's results demonstrate that the performance of the bearingless CFF can be enhanced by modifying the geometry of the casing walls, without altering the rotor or the bearingless motor. To balance the advantages of increased critical speeds with the disadvantages of reduced fluid flow, especially in industrial applications where maximising fluid performance is crucial, future research should focus on developing hybrid approaches that combine rotor stiffening with fluid dynamic enhancements. Potential solutions could include the use of advanced materials that provide both stiffness and fluid dynamic performance, the redesign of the CFF blades, or the integration of rotor dynamic solutions that do not negatively impact the CFF's fluid dynamics.

**Author Contributions:** Conceptualisation, I.B., D.S. and T.N.; methodology, I.B. and D.S.; investigation and validation, I.B.; writing—original draft preparation, I.B.; writing—review and editing, I.B., D.S., T.N. and J.W.K.; supervision, D.S. and J.W.K.; project administration, J.W.K. All authors have read and agreed to the published version of the manuscript.

**Funding:** This research was funded by the Swiss Innovation Agency Innosuisse (funding number is 46738).

**Data Availability Statement:** The data presented in this study are available upon request from the corresponding author. The data are not publicly available due to internal policies of the industry research partner.

**Acknowledgments:** The authors gratefully thank the Swiss Innovation Agency Innosuisse for their financial support and Levitronix GmbH for their financial, scientific, and technical contributions.

**Conflicts of Interest:** Daniel Steinert and Thomas Nussbaumer were employed by the company Levitronix GmbH. The remaining authors declare that the research was conducted in the absence of any commercial or financial relationships that could be construed as a potential conflict of interest.

## Nomenclature

The following abbreviations and symbols are used in this manuscript:

### Abbreviations

ArF	Argon fluoride
CFF	Cross-flow fan

CFD	Computational fluid dynamics
DUV	Deep ultraviolet
HVAC	Heating, ventilation, and air conditioning
KrF	Krypton fluoride
SPIV	Stereo particle image velocimetry
<b>Symbols</b>	
$c$	absolute velocity
$d_{\text{CFF}}$	CFF diameter
$d_{\text{rod}}$	reinforcing rod diameter
$D_{\text{rods}}$	diameter of circularly arranged rods
$d_{\text{shaft}}$	reinforcing shaft diameter
$h$	outlet height
$L_{\text{CFF}}$	CFF length
$n$	rotational speed
$Q$	fluid flow
$u$	circumferential velocity
$w$	relative velocity
$\alpha$	vortex wall inlet angle
$\beta$	vortex wall outlet angle
$\Delta p_{\text{th}\infty}$	total pressure increase
$\Delta p_{\text{th},14}$	total pressure increase from CFF first to second stage
$\Delta p_{\text{loss}}$	pressure losses
$\Delta \varphi_{\text{CFF,max}}$	maximum change in dimensionless flow
$\epsilon_1$	distance from CFF to vortex wall
$\epsilon_2$	inlet distance from CFF to rear wall
$\rho$	density
$\phi_i$	inlet angle
$\varphi_{\text{CFF}}$	dimensionless flow coefficient
$\psi_{\text{stat,CFF}}$	dimensionless pressure coefficient

## References

1. Bagaric, I.; Hu, R.; Steinert, D.; Nussbaumer, T.; Kolar, J.W. Comparative Evaluation of High-Speed Bearingless Cross-Flow Fan Designs for Lithography Excimer Lasers. *Machines* **2023**, *11*, 611. [\[CrossRef\]](#)
2. Borisov, V.M.; El'tsov, A.V.; Khristoforov, O.B. High-power, highly stable KrF laser with a pulse repetition rate. *Quantum Electron.* **2015**, *45*, 691–696. [\[CrossRef\]](#)
3. Tsushima, H.; Katsuumi, H.; Ikeda, H.; Asayama, T.; Kumazaki, T.; Kurosu, A.; Ohta, T.; Kakizaki, K.; Matsunaga, T.; Mizoguchi, H. Extremely long life and low-cost 193 nm excimer laser chamber technology for 450 mm wafer multipatterning lithography. In Proceedings of the Optical Microlithography XXVII (SPIE), San Jose, CA, USA, 4 April 2014; Volume 9052, pp. 411–418. [\[CrossRef\]](#)
4. Kakizaki, K.; Sasaki, Y.; Inoue, T.; Sakai, Y. High-repetition-rate (6 kHz) and long-pulse-duration (50 ns) ArF excimer laser for sub-65 nm lithography. *Rev. Sci. Instrum.* **2006**, *77*, 035109. [\[CrossRef\]](#)
5. Bagaric, I.; Steinert, D.; Nussbaumer, T.; Kolar, J.W. Supercritical Operation of Bearingless Cross-Flow Fan. *Machines* **2024**, *12*, 223. [\[CrossRef\]](#)
6. Tang, E.; Han, B.; Zhang, Y. Optimum compensator design for the flexible rotor in magnetically suspended motor to pass the first bending critical speed. *IEEE Trans. Ind. Electron.* **2015**, *63*, 343–354. [\[CrossRef\]](#)
7. Hu, Y.; Yang, K.; Wu, H.; Guo, X.; Wang, N. Critical Vibration and Control of the Maglev High-Speed Motor Based on  $\mu$ -Synthesis Control. *Sensors* **2022**, *22*, 8692. [\[CrossRef\]](#)
8. Ran, S.; Hu, Y.; Wu, H.; Cheng, X. Resonance Vibration Control for AMB Flexible Rotor System Based on  $\mu$ -Synthesis Controller. *Math. Probl. Eng.* **2018**, *2018*, 4362101. [\[CrossRef\]](#)
9. Wang, P.; Zhu, C. Active vibration control of a non-collocated AMBs flexible rotor system to pass the first bending critical speed. In Proceedings of the IEEE 22nd International Conference on Electrical Machines and Systems (ICEMS), Harbin, China, 11–14 August 2019; pp. 1–6. [\[CrossRef\]](#)
10. Lazzaretto, A. A criterion to define cross-flow fan design parameters. *J. Fluids Eng.* **2003**, *125*, 680–683. [\[CrossRef\]](#)
11. Toffolo, A. On the theoretical link between design parameters and performance in cross-flow fans: A numerical and experimental study. *Comput. Fluids* **2005**, *34*, 49–66. [\[CrossRef\]](#)
12. Toffolo, A. On cross-flow fan theoretical performance and efficiency curves: An energy loss analysis on experimental data. *J. Fluids Eng.* **2004**, *126*, 743–751. [\[CrossRef\]](#)
13. Toffolo, A.; Lazzaretto, A.; Martegani, A.D. An experimental investigation of the flow field pattern within the impeller of a cross-flow fan. *Exp. Therm. Fluid Sci.* **2004**, *29*, 53–64. [\[CrossRef\]](#)

14. Dang, T.Q.; Bushnell, P.R. Aerodynamics of cross-flow fans and their application to aircraft propulsion and flow control. *Prog. Aerosp. Sci.* **2009**, *45*, 1–29. [[CrossRef](#)]
15. Himeur, R.M.; Khelladi, S.; Ait Chikh, M.A.; Vanaei, H.R.; Belaidi, I.; Bakir, F. Towards an accurate aerodynamic performance analysis methodology of cross-flow fans. *Energies* **2022**, *15*, 5134. [[CrossRef](#)]
16. Kim, J.W.; Ahn, E.Y.; Oh, H.W. Performance prediction of cross-flow fans using mean streamline analysis. *Int. J. Rotating Mach.* **2005**, *2005*, 965649. [[CrossRef](#)]
17. Ouyang, H.; Tian, J.; Li, Y.; Zheng, Z.; Du, Z. Internal flow and noise investigations about the cross-flow fan with different blade angles. *J. Turbomach.* **2012**, *134*, 051023. [[CrossRef](#)]
18. Adanta, D.; Hindami, R.; Siswantara, A.I. Blade depth investigation on cross-flow turbine by numerical method. In Proceedings of the IEEE 4th International Conference on Science and Technology (ICST), Yogyakarta, Indonesia, 7–8 August 2018; pp. 1–6. [[CrossRef](#)]
19. Li, Y.; Ouyang, H.; Tian, J.; Du, Z.; Zheng, Z. Experimental and numerical studies on the discrete noise about the cross-flow fan with block-shifted impellers. *Appl. Acoust.* **2010**, *71*, 1142–1155. [[CrossRef](#)]
20. Sampat, D.L.; Govardhan, M. Computational Studies of Flow through Cross Flow Fan: Effect of Casing Parameters. *Int. J. Fluid Mech. Res.* **2012**, *39*, 54–74. [[CrossRef](#)]
21. Li, J.; Hou, Y.; Liu, J.; Wang, Z.; Li, F. Window purifying ventilator using a cross-flow fan: Simulation and optimization. *Build. Simul.* **2016**, *9*, 481–488. [[CrossRef](#)]
22. Ciocanea, A.; Marin, A.; Buretea, D.L. The influence of housing on the internal flow of a cross flow fan impeller. In Proceedings of the IEEE 2019 International Conference on Energy and Environment (CIEM), Timisoara, Romania, 17–18 October 2019; pp. 464–468. [[CrossRef](#)]
23. Shih, Y.C.; Tamilarasan, S.; Chen, P.H.; Tsao, C.C.; Lin, C.H. Optimal thermohydraulic design of the indoor unit of a split-type air conditioner. *Appl. Therm. Eng.* **2022**, *211*, 118502. [[CrossRef](#)]
24. Sun, K.; Ouyang, H.; Tian, J.; Wu, Y.; Du, Z. Experimental and numerical investigations on the eccentric vortex of the cross flow fan. *Int. J. Refrig.* **2015**, *50*, 146–155. [[CrossRef](#)]
25. Zou, T.; Zhan, D.; Hu, X.; Hu, S.; Li, Y. Experimental and numerical study of cross-flow fan in air-conditioner indoor unit. *Int. J. Refrig.* **2022**, *141*, 102–111. [[CrossRef](#)]
26. Cai, X.; Zhang, C.; Wang, B. Numerical Study on Fluid Dynamic Characteristics of a Cross-Flow Fan. *J. Mar. Sci. Eng.* **2023**, *11*, 846. [[CrossRef](#)]
27. Shih, Y.C.; Hou, H.C.; Chiang, H. On similitude of the cross flow fan in a split-type air-conditioner. *Appl. Therm. Eng.* **2008**, *28*, 1853–1864. [[CrossRef](#)]
28. Özer, Ö.; Kumlutaş, D. Experimental investigation on cross flow fan’s casing parameters inside of a split air conditioner indoor unit by Stereo Particle Image Velocimetry. *Appl. Therm. Eng.* **2017**, *124*, 1233–1246. [[CrossRef](#)]
29. Vanaei, H.R.; Khelladi, S.; Dobrev, I.; Bakir, F.; Himeur, R.M.; Mammeri, A.; Azzouz. Performance and Efficiency of Cross-Flow Fans—A Review. *Energies* **2023**, *16*, 7798. [[CrossRef](#)]
30. Zhang, W.; Yuan, J.; Si, Q.; Fu, Y. Investigating the In-Flow Characteristics of Multi-Operation Conditions of Cross-Flow Fan in Air Conditioning Systems. *Processes* **2019**, *7*, 959. [[CrossRef](#)]
31. Gan, J.; Liu, F.; Liu, M.; Wu, K. The unsteady fluctuating pressure and velocity in a cross flow fan. *J. Therm. Sci.* **2008**, *17*, 349–355. [[CrossRef](#)]

**Disclaimer/Publisher’s Note:** The statements, opinions and data contained in all publications are solely those of the individual author(s) and contributor(s) and not of MDPI and/or the editor(s). MDPI and/or the editor(s) disclaim responsibility for any injury to people or property resulting from any ideas, methods, instructions or products referred to in the content.